Finite frequency tomography of D″ shear velocity heterogeneity beneath the Caribbean

Shu-Huei Hung,[1] Edward J. Garnero,[2] Ling-Yun Chiao,[3] Ban-Yuan Kuo,[4] and Thorne Lay[5]

Received 4 August 2004; revised 1 February 2005; accepted 22 April 2005; published 28 July 2005.

[1] The shear velocity structure in the lowermost 500 km of the mantle beneath the Caribbean and surrounding areas is determined by seismic tomography applied to a suite of *Sd*-*SKS*, *ScS*-*S*, (*Scd* + *Sbc*)-*S*, and *ScS*-(*Scd* + *Sbc*) differential times, where (*Scd* + *Sbc*) is a pair of overlapping triplication arrivals produced by shear wave interaction with an abrupt velocity increase at the top of the D″ region. The inclusion of the triplication arrivals in the inversion, a first for a deep mantle tomographic model, is possible because of the widespread presence of a D″ velocity discontinuity in the region. The improved ray path sampling provided by the triplication arrivals yields improved vertical resolution of velocity heterogeneity within and above the D″ region. The reference velocity model, taken from a prior study of waveforms in the region, has a 2.9% shear velocity discontinuity 250 km above the core-mantle boundary (CMB). Effects of aspherical structure in the mantle at shallower depths than the inversion volume are suppressed by applying corrections for several different long-wavelength shear velocity tomography models. Born-Fréchet kernels are used to characterize how the finite frequency data sample the structure for all of the differential arrival time combinations; inversions are performed with and without the kernels. The use of three-dimensional kernels stabilizes the tomographic inversion relative to a ray theory parameterization, and a final model with 60- and 50-km correlation lengths in the lateral and radial dimensions, respectively, is retrieved. The resolution of the model is higher than that of prior inversions, with 3–4% velocity fluctuations being resolved within what is commonly described as a circum-Pacific ring of high velocities. A broad zone of relatively high shear velocity material extends throughout the lower mantle volume beneath the Gulf of Mexico, with several percent lower shear velocities being found beneath northern South America. Concentrated low-velocity regions extend through the D″ layer under the Caribbean, Colombia, and Ecuador, suggestive of small-scale plumes in the boundary layer and possible lateral variations of the D″ discontinuity. One scenario consistent with the imaged features involves subducted Farallon plate ponding at the base of the mantle and laterally displacing hot boundary layer material that piles up and destabilizes on its margins.

Citation: Hung, S.-H., E. J. Garnero, L.-Y. Chiao, B.-Y. Kuo, and T. Lay (2005), Finite frequency tomography of D″ shear velocity heterogeneity beneath the Caribbean, *J. Geophys. Res.*, *110*, B07305, doi:10.1029/2004JB003373.

1. Introduction

[2] The deep mantle below circum-Pacific margins has long been characterized as having higher than average shear velocities [e.g., *Dziewonski and Woodhouse*, 1987; *Tanimoto*, 1990], an attribute that has commonly been linked to the 200 Myr long history of oceanic plate subduction beneath most of these margins [e.g., *Lithgow-Bertelloni and Richards*, 1998]. As mantle tomographic images have improved, the inference that subducted slab material penetrates into the deep mantle and is the source of the high shear velocity patterns has been advanced increasingly forcefully [e.g., *Grand et al.*, 1997; *Grand*, 2002], although in some regions there does not appear to be continuity of high-velocity features to deep in the mantle [e.g., *Fukao et al.*, 2001]. Improved spatial resolution near the base of the mantle has led to recognition that the circum-Pacific "ring" of high-velocity material is not necessarily a laterally coherent structure but rather one with significant

[1]Department of Geosciences, National Taiwan University, Taipei, Taiwan.
[2]Department of Geological Sciences, Arizona State University, Tempe, Arizona, USA.
[3]Institute of Oceanography, National Taiwan University, Taipei, Taiwan.
[4]Institute of Earth Sciences, Academia Sinica, Nankang, Taiwan.
[5]Institute of Geophysics and Planetary Physics, Earth Sciences Department, University of California, Santa Cruz, California, USA.

0148-0227/05/2004JB003373$09.00

patchiness and intermittent high and low velocities on scale lengths of 500 to 1000 km [e.g., *Castle et al.*, 2000; *Kuo et al.*, 2000; *Megnin and Romanowicz*, 2000; *Ritsema and van Heijst*, 2000; *Gu et al.*, 2001; *Wysession et al.*, 2001; *Grand*, 2002; *Fisher et al.*, 2003; *Montelli et al.*, 2004]. Establishing the detailed shear velocity structure beneath a region that may have descending midmantle flow is essential for advancing our understanding of mantle dynamics, the fate of slabs, a lower mantle postperovskite phase transition, and chemical mixing of mantle thermochemical heterogeneities.

[3] This study seeks to improve the spatial resolution of shear velocity structure in the deep mantle beneath the Caribbean, Gulf of Mexico, Central America, and northern South America. This area is well sampled by shear waves from South America subduction zone earthquakes recorded by broadband seismic stations in North America. As is the case for most of the deep mantle, the ray path coverage has very limited azimuthal sampling; however, extensive coverage of this region can be obtained using several different shear wave phases. The shear velocity structure in this region is generally higher than average in global mantle and D″ tomographic images, in fact, some of the highest velocities in all of the lower mantle are in this region. In addition, prior work has established that an abrupt increase in shear velocity occurs about 250 km above the core-mantle boundary (CMB) across much, if not all, of the region [e.g., *Lay and Helmberger*, 1983; *Kendall and Nangini*, 1996; *Ding and Helmberger*, 1997; *Garnero and Lay*, 2003; *Lay et al.*, 2004a]. The existence of this velocity increase near the top of the D″ region is inferred from *S* wave arrivals that precede *ScS*, the reflection from the CMB. While there is likely some lateral variation in the depth and velocity contrast of the discontinuity [e.g., *Lay et al.*, 2004a; *Thomas et al.*, 2004], it appears that the average structure in the region is quite well characterized with a 2% to 3% velocity increase from 200 to 300 km above the CMB.

[4] We use a large data set of carefully measured shear wave differential times, including measurements of phases generated by the D″ discontinuity, in a high-resolution regional-scale tomographic inversion for shear velocity structure in the lowermost 500 km of the mantle beneath the Caribbean. Three-dimensional kernels [e.g., *Dahlen et al.*, 2000; *Hung et al.*, 2000; *Zhao et al.*, 2000] are used in the inversion to account for finite frequency effects, and the resulting regional model has the highest resolution yet obtained for the deep mantle by tomography. In the following, we introduce our data, finite frequency and inversion methodology, and results. Our models are compared to those from infinite frequency (ray theory) tomography. Finally, we interpret our results and discuss resolution and uncertainties.

2. Data, Methodology and Model Parameterization

2.1. Differential Travel Time Residuals

[5] Differential travel times for broadband shear waves from digital Global Seismic Network, Berkeley Digital Seismic Network, TERRAscope/Trinet, Canadian National Seismic Network, and long-period analog World Wide Seismographic Station Network (WWSSN) recordings compiled by *Garnero and Lay* [2003] are utilized for imaging shear velocity variations in the lowermost mantle beneath the Caribbean and Central America. Data from 61 earthquakes in the depth range 100 to 650 km with seismic magnitudes from 5.5 to 6.9 are used. The data were selected based on good signal-to-noise ratio and waveforms indicative of simple source processes. All measurements from digital data were made on signals that have been deconvolved by the instrument response to obtain ground displacements with mild bandpass filtering between 1 and 100 s. The data were corrected for splitting effects of upper mantle anisotropy prior to rotation to the great circle reference frame (see *Garnero and Lay* [2003] for details). Transverse components were used for all measurements other than those involving *SKS* phases. Differential times are used rather than absolute times in order to minimize the contributions from upper mantle heterogeneities beneath the receivers and in the source regions, as well as source mislocation errors.

[6] The measurements were made for (1) differential times between *S* (or the diffracted phase, *Sd*) on the transverse and *SKS* on the longitudinal components; (2) differential times between *ScS* and *S*; (3) differential times between any significant lower mantle triplication arrival and *S*; and (4) differential times between *ScS* and any significant lower mantle triplication arrival. The triplications arrivals, identified on the basis of their timing and move out between *S* and *ScS*, are interpreted as the interference between triplication energy that dives below a D″ velocity discontinuity (*Scd*, in the terminology of *Lay and Helmberger* [1983]) and energy that reflects off of the discontinuity (*Sbc*). *Scd* and *Sbc* arrive within a second or two of one another. Measuring the peak arrival time of the interfering *Scd* + *Sbc* arrivals is the best option given the 5–10 s predominant periods of our data, and we will treat this pair of arrivals as a single interference arrival in our tomographic modeling. This overlapping *Scd* + *Sbc* energy is typically weak at distances less than about 77 degrees, but increases with distance to be as strong as *ScS* by 81 degrees, although it arrives only a few seconds after direct *S* (*Sab*). Beyond about 85 degrees *Scd* is the first arrival, and one can measure *Sab*-*Scd* differential times at distances greater than 90 degrees, but we exclude these measurements from the tomographic imaging due to strong dependence of the ray paths on the reference model. Because the waveforms have simple pulses but little time separation in many cases, measurements are made based on peak-to-peak values (rather than by cross correlation) for all times except those of *Sd*-*SKS*, where onset times were picked. The final data set includes 327 *S*(*Sd*)-*SKS*, 297 *ScS*-*S*, 98 (*Scd* + *Sbc*)-*S* and 98 *ScS*-(*Scd* + *Sbc*) differential travel times. The *S*-*SKS* and *ScS*-*S* data used in this study directly correspond to those used by *Garnero and Lay* [2003], and general characteristics of the overall data set are illustrated and described in further detail in that paper.

[7] The ray paths for our data set dive into the lower mantle beneath the Caribbean and Central America. The upper portion of the lower mantle in this region has tabular high-velocity structures in both *P* and *S* wave tomographic models [*Grand et al.*, 1997], which shallow portions of our paths may encounter, but are insufficient to directly image. The lowermost mantle is well sampled by the combined

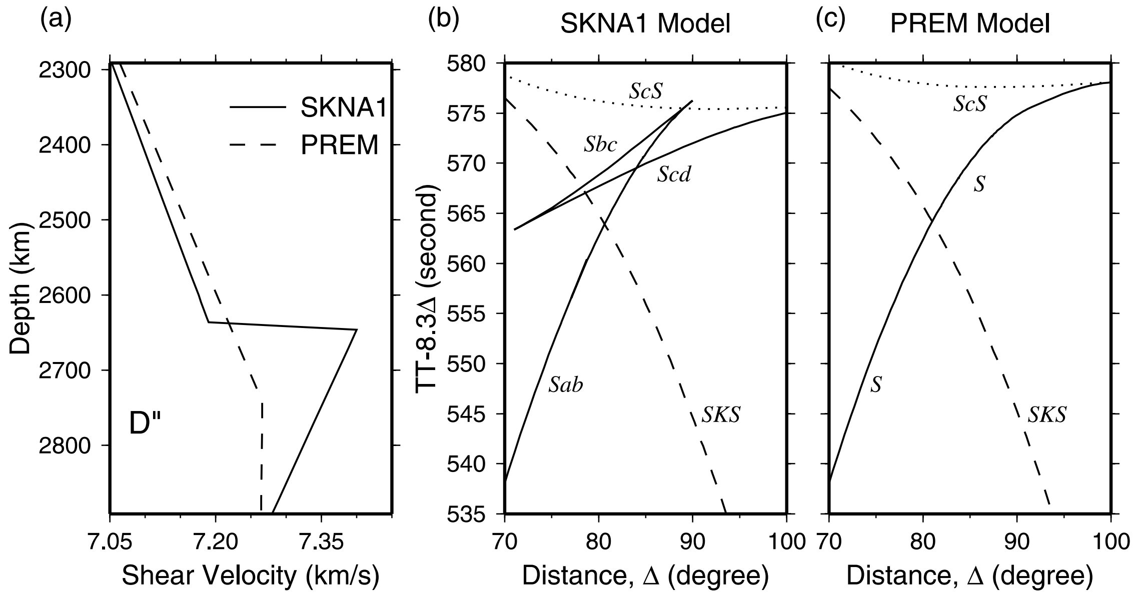

Figure 1. (a) Radially symmetric Earth models SKNA1 and PREM. There is an abrupt velocity increase at the top of a 250-km-thick D″ layer for SKNA1. (b) Travel time curves of *ScS*, *SKS*, and triplication arrivals *Sab*, *Scd*, and *Sbc* phases for model SKNA1. (c) Travel time curves of *S*, *SKS*, and *ScS* phases for PREM model.

coverage of our *SKS*, *Sd*, *ScS*, and *Scd* + *Sbc* phases, and we design the study to image the deep mantle structure. The tomographic domain is a 500 km thick spherical shell sitting atop the CMB that laterally spans the area of five icosahedrons centered beneath the Caribbean. To remove the contributions to the differential travel times associated with mantle heterogeneity outside the study region we separately apply travel time corrections to the raw data computed for global shear velocity models from *Ritsema and van Heijst* [2000], *Grand* [2002] and *Megnin and Romanowicz* [2000], hereafter referred to CIT, UT and UCB, respectively. Comparison of the results for different aspherical models allows us to assess the robustness of the deep mantle model we seek.

[8] As mentioned above, most global tomographic inversions find high S velocity in the lower mantle beneath the Caribbean, but the velocity variations in these models tend to be too gradual to cause triplication of the S wave front. Thus, without arbitrarily augmenting the velocity heterogeneity in the models, we cannot produce arrivals corresponding to the *Scd* + *Sbc* energy [see *Ni et al.*, 2000]. Inclusion of these phases in the tomographic inversion requires associated ray paths, and simply assuming artificial reflection horizons in a smooth model leads to problems with matching the behavior of actual triplication arrivals. Travel time analysis and waveform modeling suggest that the one-dimensional (1-D) model from *Kendall and Nangini* [1996], SKNA1, which has a 2.9% D″ shear velocity discontinuity 250 km above the CMB and a mild negative velocity gradient within D″ (Figure 1), produces correct triplication behavior of the wave field. Standard reference structures, such as the PREM model [*Dziewonski and Anderson*, 1981] cannot produce such triplication behavior. The SKNA1 model is reasonably representative of structure across the broad region of the deep mantle beneath the Caribbean [e.g., *Garnero and Lay*, 2003]. We therefore adopt SKNA1 as a reference structure and invert differential residual data for shear velocity variations in our model volume relative to SKNA1. The dependency of our results on reference structure will be discussed later.

[9] Histogram distributions of all measured differential travel time residuals for each of the three sets of aspherical model corrections are shown in Figure 2. These anomalies are obtained from the observed differential travel times by subtracting the predicted differential times for the SKNA1 model (applying aspherical structure corrections along ray paths between the surface and 500 km above the CMB). The corrected travel time residuals based on the CIT, UT and UCB models all yield nearly Gaussian distributions with means close to zero. There are some large positive residuals in all three data sets, which may suggest not all structure in the study region is high velocity, as portrayed in the long-wavelength tomographic models.

[10] Figure 3 shows the ray path coverage of four subsets of differential travel time residuals, (*Scd* + *Sbc*)-*S*, *ScS*-(*Scd* + *Sbc*), *ScS*-*S*, and *S*(*Sd*)-*SKS* using the SKNA1 model for path geometry prediction. Only the ray segments within the lowermost 500 km of the mantle are highlighted in Figure 3. In addition to the relatively widespread ray coverage provided by *S*(*Sd*)-*SKS* and *ScS*-*S* data sets, the triplication arrivals have bottoming depths which directly sample the D″ region beneath the Gulf of Mexico and the Caribbean. Given that it has the highest sampling density, this region is best resolved in our tomographic study and associated solution structure is emphasized in later discussion.

[11] Individual differential residuals relative to model SKNA1 are plotted in Figure 4 at the midpoints of the ray paths projected on the surface. The variations in the resid-

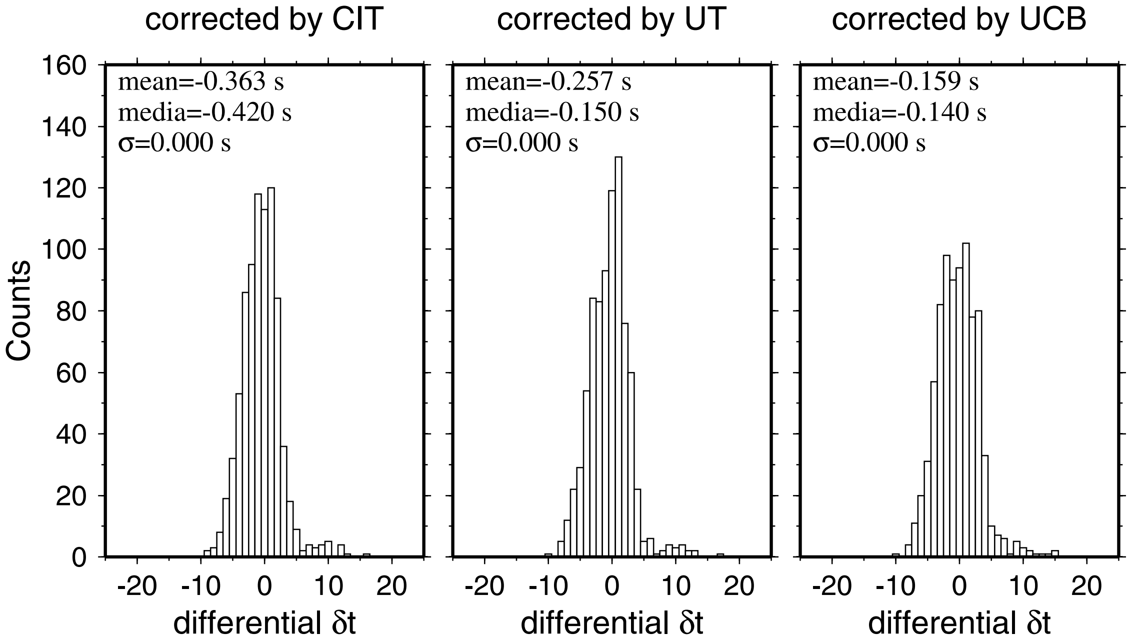

Figure 2. Histograms showing the distribution of differential travel time anomalies relative to model SKNA1. The data include *ScS-S*, *S*(*Sd*)-*SKS*, (*Scd* + *Sbc*)-*S*, and *ScS*-(*Scd* + *Sbc*) differential time residuals after the removal of travel time advances or delays related to mantle heterogeneity outside the lowermost 500 km of the mantle. Three global models are used for separate path corrections, as described in the text.

uals show some spatially coherent patterns that indicate the presence of small-scale velocity heterogeneity in the D″ region. Correction of the data for the three different tomographic models results in very similar spatial patterns, and we can anticipate that only minor differences will be found in our tomographic solution models based on the different sets of corrections.

2.2. Ray Theory Versus Finite Frequency Theory

[12] In conventional seismic tomography based on linearized ray theory, a differential travel time shift of two phases A and B, $\delta(t_A - t_B)$, relative to that predicted by a radially symmetric Earth model such as PREM or SKNA1 is obtained by the difference of the integration of the first-order perturbation of slowness along each individual geometrical ray path,

$$\delta(t_A - t_B) = -\int_{\mathbf{s}\,A}^{\mathbf{r}} \frac{1}{\beta(x)}\left(\frac{\delta\beta}{\beta}\right)dx + \int_{\mathbf{s}\,B}^{\mathbf{r}} \frac{1}{\beta(x)}\left(\frac{\delta\beta}{\beta}\right)dx, \quad (1)$$

where dx is the incremental arc length along the ray path for phase A or phase B from the source $\mathbf{s}$ to the receiver $\mathbf{r}$, $\beta(x)$ is the unperturbed shear wave speed in the 1-D reference Earth model at a point x on the ray path, and $\delta\beta/\beta$ is the fractional shear wave speed perturbation at x to be imaged.

[13] The finite frequency approach relies on 3-D Born-Fréchet kernels (often called banana-doughnut kernels [see *Hung et al.*, 2001]) and expresses a travel time shift measured by cross correlation of an observed seismogram with the corresponding spherical Earth synthetic as the integral of volumetric sensitivity with fractional wave speed perturbations over the entire Earth's mantle. A differential travel time residual determined by cross correlation of two phase arrivals which have similar pulse shapes and ray paths near the source and the receiver has a Fréchet kernel that is simply the difference of the individual Fréchet kernels [*Dahlen et al.*, 2000],

$$\delta(t_A - t_B) = \iiint_{\oplus} (K_A(\mathbf{x}) - K_B(\mathbf{x}))\left(\frac{\delta\beta}{\beta}\right) d^3\mathbf{x}. \quad (2)$$

The quantities $K_A(\mathbf{x})$ and $K_B(\mathbf{x})$ are the values of 3-D Fréchet kernels at a point $\mathbf{x}$ for the individual travel time shifts δt_A or δt_B, respectively. Similarly, $\delta\beta/\beta$ is the fractional shear wave speed perturbation at $\mathbf{x}$ in the Earth's mantle to be imaged.

[14] Ray theoretical representation of Fréchet kernels involves the double sum of all the propagating composite source-to-scatterer and scatterer-to-receiver body waves that deviate from the geometrical ray path. Taking advantage of the fact that the contribution to the 'exact' travel time kernel mainly comes from like-type forward scattering paths (often referred to as paraxial rays) in the vicinity of the unperturbed ray path, a practical formulation for computing K efficiently is the paraxial kernel given by [*Dahlen et al.*, 2000; *Hung et al.*, 2000]:

$$K = -\frac{1}{2\pi c}\left(\frac{\mathcal{R}}{c_r\mathcal{R}'\mathcal{R}''}\right)\frac{\int_0^\infty \omega^3|s_{syn}(\omega)|^2\sin(\omega\Delta T)\,d\omega}{\int_0^\infty \omega^2|s_{syn}(\omega)|^2 d\omega}, \quad (3)$$

where ΔT is the additional travel time required to take the detour path to a point scatterer; that is, the integration point $\mathbf{x} = (r, \theta, \phi)$ in equation (2) within a spherically

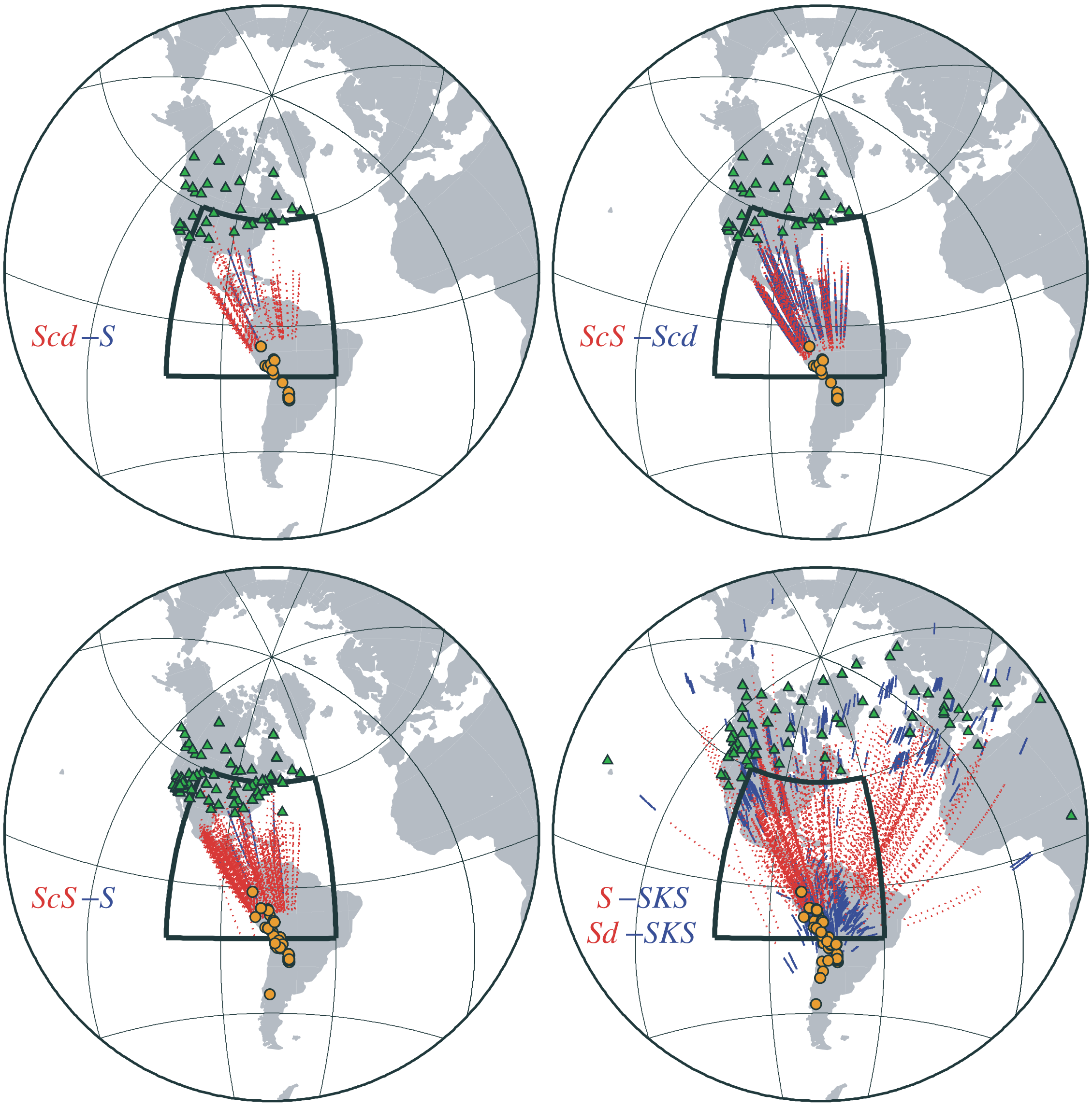

Figure 3. Projection of great circle paths for (*Scd* + *Sbc*)-*S*, *ScS*-(*Scd* + *Sbc*), *ScS*-*S*, and *S*(*Sd*)-*SKS* differential travel time residuals using the SKNA1 model for ray geometry prediction. Only the ray segments in the lowermost 500-km mantle are highlighted. Solid circles and triangles represent earthquake epicenters and station locations, respectively.

symmetric Earth. The scaling constants c and c_r are the wave speeds of the 1-D background model at the scatterer and receiver; the quantities $\mathcal{R}$, $\mathcal{R}'$ and $\mathcal{R}''$ are associated with the spreading factors for the unperturbed ray, the forward source-to-scatterer ray, and the backward receiver-to-scatterer ray. The power spectrum, $|s_{\mathrm{syn}}(\omega)|^2$, specifies the frequency content of the synthetic for an observed broadband pulse used in cross-correlation travel time measurement, which has a dominant period of 8 s for our data sets. In many circumstances, there may be more than one phase arriving within the cross-correlation time window. In the case of the triplication arrivals, *Sab* and *Scd*, used in this study, the waveform of the *Scd* phase (which turns within the D″ layer) is influenced by interference with the *Sbc* arrival (which reflects from the top of the D″ layer). The Fréchet kernels governing such a pair of interfering or overlapping phases is written as

$$
\begin{aligned}
K_{Scd+Sbc} = &-\frac{1}{2\pi c c_r D}\int_0^\infty \omega^3 |s_{\mathrm{syn}}(\omega)|^2 \\
&\cdot \Big[\left(\mathcal{R}'_{Scd}\mathcal{R}''_{Scd}\mathcal{R}_{Scd}\right)^{-1} \sin\omega\Delta T_{Scd} \\
&+ \left(\mathcal{R}'_{Scd}\mathcal{R}''_{Scd}\mathcal{R}_{Sbc}\right)^{-1} \sin\omega(\Delta T_{Scd} + T_{Scd} - T_{Sbc}) \\
&+ \left(\mathcal{R}'_{Sbc}\mathcal{R}''_{Sbc}\mathcal{R}_{Scd}\right)^{-1} \sin\omega(\Delta T_{Sbc} + T_{Sbc} - T_{Scd}) \\
&+ \left(\mathcal{R}'_{Sbc}\mathcal{R}''_{Sbc}\mathcal{R}_{Sbc}\right)^{-1} \sin\omega\Delta T_{Sbc} \Big] d\omega, \qquad (4)
\end{aligned}
$$

where

$$
\begin{aligned}
D = &\int_0^\infty \omega^2 |s_{\mathrm{syn}}(\omega)|^2 \\
&\cdot \left[\mathcal{R}_{Scd}^{-2} + \mathcal{R}_{Sbc}^{-2} + 2\mathcal{R}_{Scd}^{-1}\mathcal{R}_{Sbc}^{-1}\cos\omega(T_{Scd} - T_{Sbc})\right] d\omega. \qquad (5)
\end{aligned}
$$

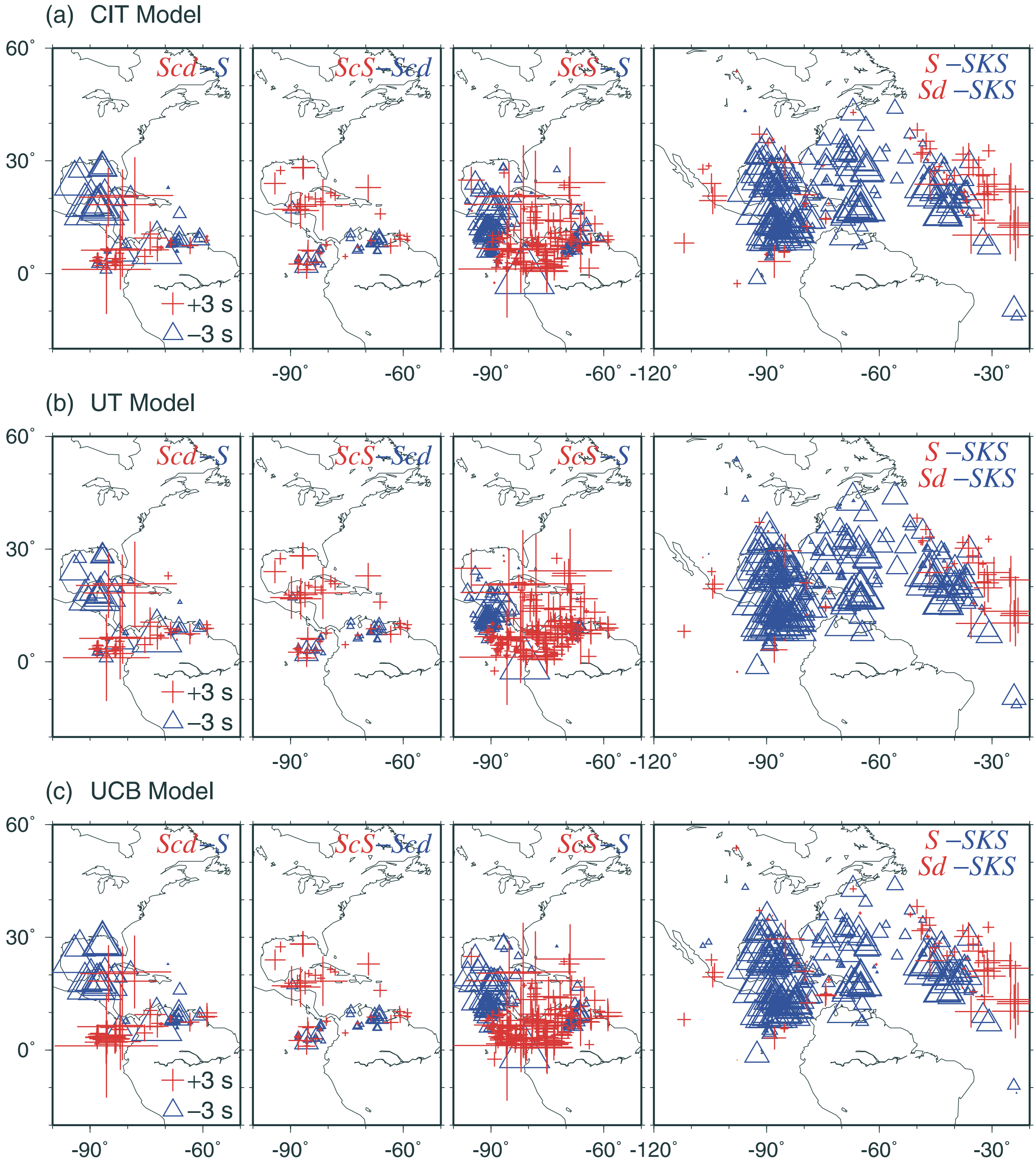

Figure 4. Differential travel time residuals for (*Scd* + *Sbc*)-*S*, *ScS*-(*Scd* + *Sbc*), *ScS*-*S*, and *S*(*Sd*)-*SKS* measurements plotted at the midpoints of the ray paths. (a) CIT, (b) UT, and (c) UCB models are used for travel time corrections for mantle heterogeneity. Size of symbols is proportional to the magnitude of the differential travel time residuals.

The quantities T_{Scd} and T_{Sbc} are the predicted travel times for *Scd* and *Sbc* phases from the source **s** to the receiver **r** in the SKNA1 model; ΔT_{Scd} and ΔT_{Sbc} are the additional travel times required by the detour paths of the scattered *Scd* and *Sbc* arrivals through a single point scatterer of heterogeneity; that is, the integration point **x** in equation (2). The scaling constants c and c_{r} are shear wave speeds of the 1-D background model at the scatterer **x** and receiver **r**; the quantities of $\mathcal{R}$, $\mathcal{R}'$, and $\mathcal{R}''$ with subscripts *Scd* and *Sbc* are geometrical spreading factors for the unperturbed ray, the forward source-to-scatterer ray, and the backward receiver-to-scatterer ray, for *Scd* and *Sbc* phases, respectively. Figure 5 illustrates the paraxial Fréchet kernels on various 2-D cross sections for travel time shifts measured by

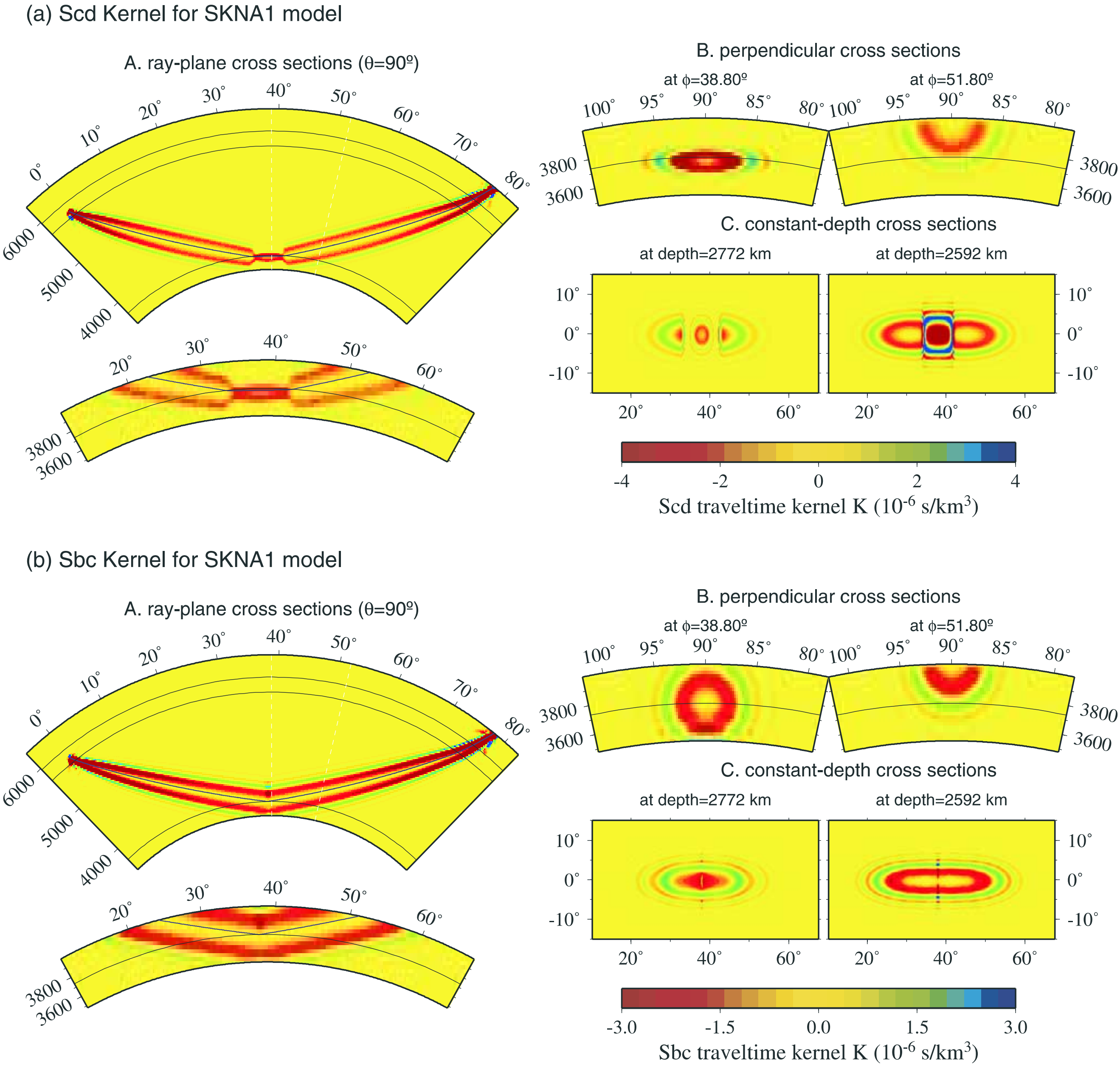

Figure 5. (a) Sensitivity of a finite frequency travel time shift determined by the waveform of an isolated *Scd* phase from an earthquake 561 km deep recorded at an epicentral distance $\Delta = 78°$. (b) Sensitivity of a finite frequency travel time shift determined by the waveform of an isolated *Sbc* phase from the same event and station.

the individual waveform of the (1) *Scd* or (2) *Sbc* phase only. Figure 6a shows the sensitivity kernel for a finite frequency travel time shift determined by the interfering waveform of overlapping *Scd* and *Sbc* phases. Figure 6b displays the differential kernel for *ScS*-(*Scd* + *Sbc*) residuals, simply the difference of individual *ScS* and interfering *Scd* + *Sbc* sensitivity kernels.

2.3. Model Parameterization

[15] Similar to *Chiao and Kuo* [2001], our model of shear velocity perturbation is parameterized in vertexes of 3-D spherical triangular-shaped voxels (cells) that totally span five geodesic icosahedrons centered at (290°E, 23°N) with a total thickness of 500 km in the lowermost mantle. Five spherical triangles with almost equal spherical areas are successively refined by taking midpoints on the edges to form four subtriangles. Refining through six levels yields a tessellation of 5120 spherical triangles with approximate dimension of $0.71° \times 0.71°$ connected by 2805 vertexes. The 500-km-thick spherical shell is then divided into sixteen layers of constant thickness of ~31 km, resulting in a total of 81920 voxels and 47685 vertexes (Figure 7).

[16] In travel time tomography, only a finite amount of observed data is available to invert for the values of seismic velocity perturbations at the discrete vertexes of spherical voxels. Numerical integration of equation (3) within a single

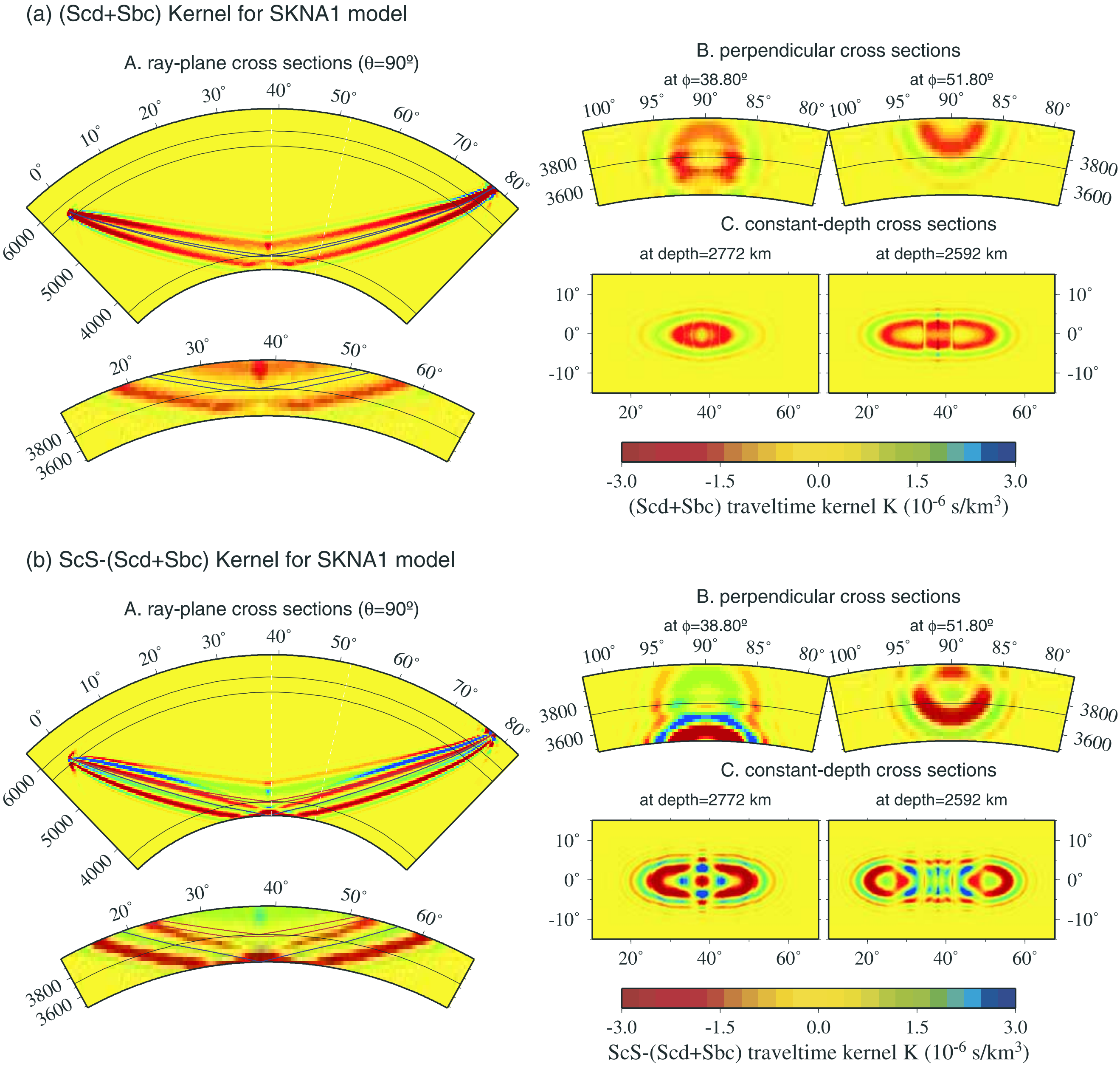

Figure 6. (a) Sensitivity of a finite frequency travel time shift determined by the waveforms of the overlapping *Scd* and *Sbc* phases for the same event and station as in Figure 5. (b) Sensitivity of the differential *ScS*-(*Scd* + *Sbc*) travel time shift measured by the waveforms of *ScS* phase and of the interfering *Scd* and *Sbc* phases for the same event and station as in Figure 5.

voxel is achieved by the weighted sum of the values at limited sampling points using the Gaussian quadrature formula [e.g., *Zienkiewicz and Taylor*, 1989] and the resulting value is distributed to all the vertexes bounding the voxel. Contributions from all the voxels are summed to yield the data equation of the form,

$$d_i = G_{ij} m_j = (g_i, m), \tag{6}$$

where d_i is the ith data in a total of N differential travel time shifts, cast as the result of the discrete inner product of the model vector $\mathbf{m} = [m_1, m_2, .., m_M]^T$ of dimension M (47685 vertexes) and the coefficient vector g_i of the same dimension with components, G_{ij} obtained from the result of the numerical integration described previously. The values can be either the difference of the total path lengths for a geometric ray theory inversion or the integrated volumetric kernel values throughout a specific volume or voxel that contributes to the jth vertex between the two arrivals in the ith-paired differential travel time measurement.

[17] In Figure 8 we use the square root of the diagonal values of the product of the Gram matrix $\mathbf{G}$ and its transpose $\mathbf{G}^T$, that is, $\sqrt{\mathrm{diag}(G^T G)}$, to indicate the overall sensitivity inherent to the kernel and ray tomography provided by the observed differential travel time data. Each element of diag($\mathbf{G}^T\mathbf{G}$) is equivalent to the total sum of the

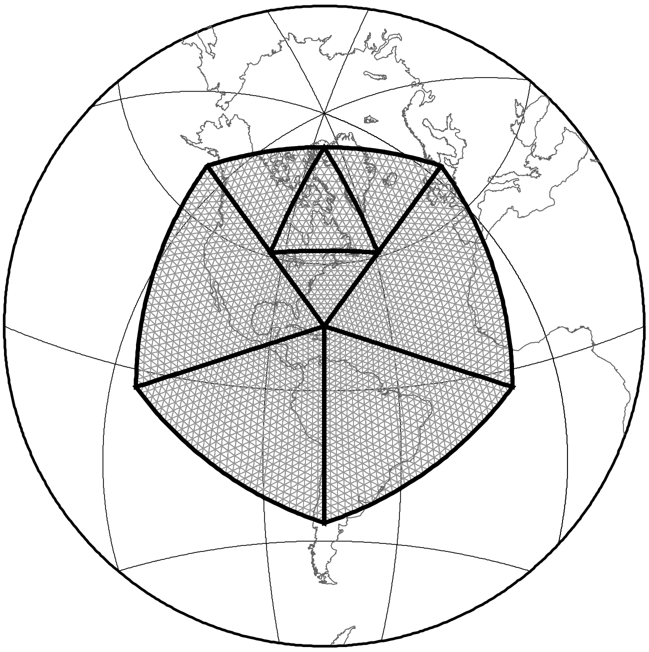

Figure 7. Configuration of the model parameterization that spans an area of 5 icosahedrons centered at (230°E, 29°N). Each spherical triangle is successively subdivided into four subtriangles.

squared values of the volumetric kernels contributing to each node or the squares of the path lengths of 1-D rays weighted by the background velocity. The variation of these values reflects the robustness of the constraint on shear velocity perturbation at each vertex. The plots are presented in a logarithm scale on eight constant depth cross sections where the resolved shear velocity anomaly is shown subsequently. As expected, sampling in the ray-based tomography is primarily defined by the path geometry while sampling by off-path sensitivity of finite frequency travel times yields a much smoother and homogenized pattern, particularly in the sub-Caribbean region which has dense data sampling.

[18] Solving the N(=820) data equations of equation (6) constrained by the N observed travel time data simultaneously would yield an estimate of the M(=47685) pursued model parameters. Because a large portion of the model parameters is unresolvable as a result of sparse or no data sampling, regularization either with minimum norm or minimum smoothing criteria is often imposed on such underdetermined problems to provide the additional constraints needed to suppress noisy small-scale variations and to acquire more robust, long-wavelength features in the models. One possible solution for the model vector $\mathbf{m}$ is the standard damped least squares (DLS) solution in which an a priori nonnegative damping factor is specified to control the degree of the minimization of model norms. Alternatively, we perform the smoothness regularization scheme rather than the simple norm damping in the DLS solution by imposing a convolutional quelling operator on equation (6). The solution is then obtained by

$$\hat{\mathbf{m}} = \mathbf{W}\left(\mathbf{W}^T\mathbf{A}^T\mathbf{A}\mathbf{W} + \theta^2\mathbf{I}\right)^{-1}\mathbf{W}^T\mathbf{A}^T\mathbf{d}, \tag{7}$$

where $\mathbf{W}$ is the convolution operator characterized by a prescribed correlation length on the resolved model [*Meyerholtz et al.*, 1989], $\mathbf{I}$ is an $M \times M$ identity matrix, and θ^2 is a nonnegative damping factor specified prior to the inversion to provide the intended harshness of the minimum norm criterion. If $\mathbf{W}$ is an identity matrix, then no a priori correlation length is imposed and the model solution becomes identical to that of the standard DLS case. We choose a Gaussian correlation function with two length scales involving the standard deviations in the lateral and radial directions.

3. Inversion Results

3.1. Models

[19] We conduct a trade-off analysis between variance reduction and model variance to determine the appropriate values of the nonnegative damping factor for the resolved models. Figure 9 shows the trade-off curves derived from the kernel- and ray-based models, respectively. In addition, model smoothing is invoked by means of prescribing stationary model correlations of one degree (~60 km at the CMB) laterally and 50 km radially. Figure 10 compares the (1) kernel-derived tomographic images with those obtained from (2) conventional ray tomography. Lateral variations in shear velocity perturbations relative to the SKNA1 model are illustrated at the eight different depths indicated to the right of each map. The UCB model is used for the travel time corrections for heterogeneity outside the model, a choice which is not critical. Models with similar data fits or variance reductions are chosen for comparison. The variance reduction corresponding to each tomographic solution model $\hat{\mathbf{m}}$ is estimated by

$$\left[1 - \frac{\sum_{i=1}^{N}\left(d_i - G_{ij}\hat{m}_j\right)^2}{\sum_{i=1}^{N} d_i^{\,2}}\right]100\%. \tag{8}$$

The selected models obtained with two different theories yield variance reductions of ~74%. Since SKNA1 has high shear velocity structure in the 250-km-thick D″ layer relative to PREM, the baseline of the tomographic model is shifted in the lower 250 km. The resolved shear velocity heterogeneity relative to PREM is thus only partially offset by some small-scale low-velocity fluctuations superimposed in the long-wavelength, relatively fast velocity D″ region (see Figure A1 in the auxiliary materials[1]). While the absolute velocities are not uniquely resolved, the very existence of the *Scd* + *Sbc* arrivals does require high velocities if the wave field is to triplicate. If the energy between *S* and *ScS* is caused by scattering from localized heterogeneities rather than specular reflections, this need not be the case. After removal of the average velocity perturbation of each layer, lateral variations in shear velocity heterogeneity relative to the PREM model are quite similar to those relative to the SKNA1 model (Figure A2), although the radial gradients in volumetric heterogeneity in this case are unlikely to be sufficient to account for the amplitudes of the phases between *S* and *ScS*. Using the same damping and smoothing regularization, the differential travel time data

[1] Auxiliary material is available at ftp://ftp.agu.org/apend/jb/2004JB003373.

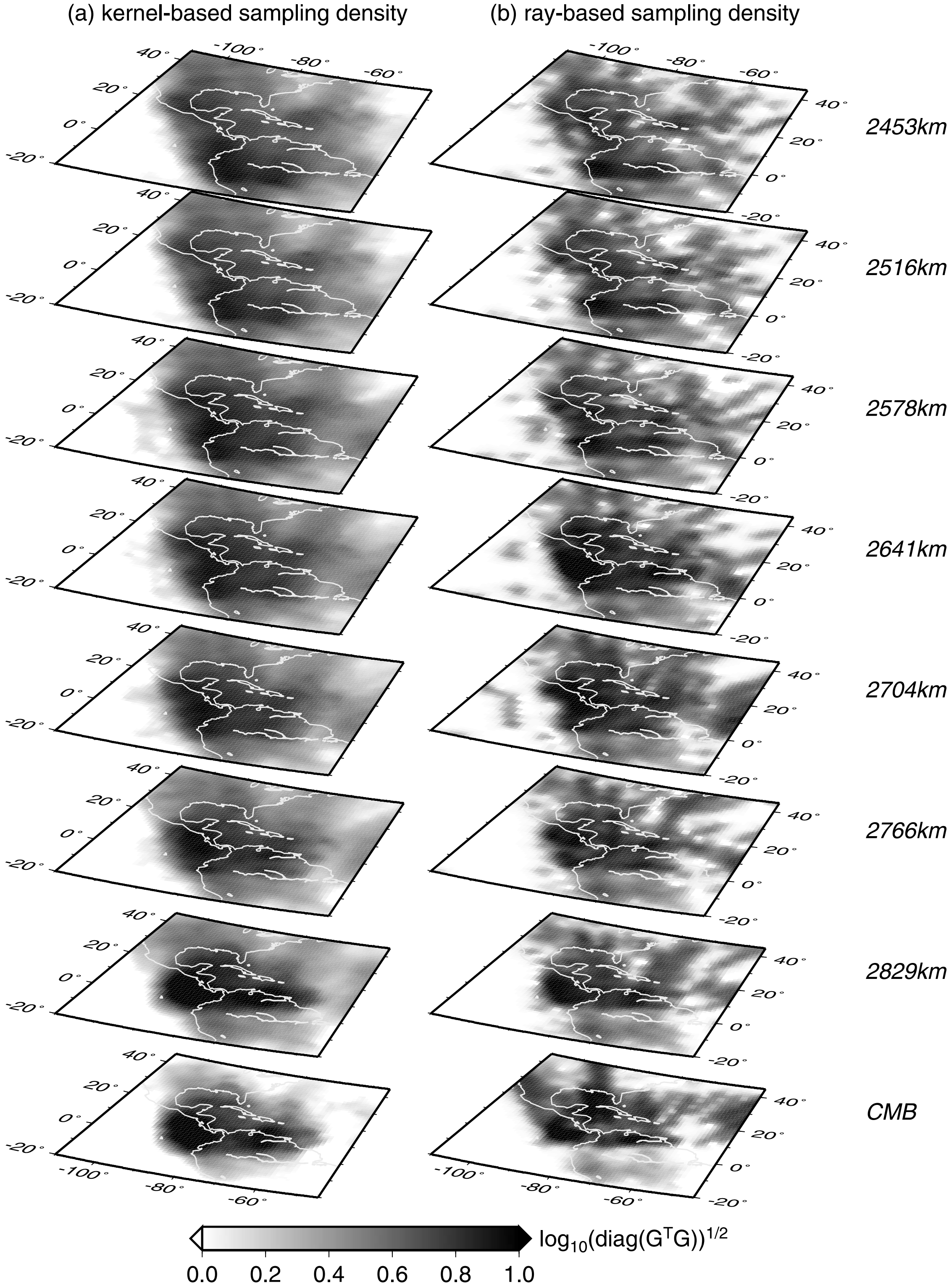

Figure 8. (a) Sampling density of all the observed differential travel time shifts based on finite frequency kernel theory. (b) Sampling density of all the observed differential travel time shifts based on geometrical ray theory.

sets corrected with different global models yield very similar shear velocity structures. This is not unexpected for several reasons: (1) the ray paths of the phases used in our differential times are extremely close in the uppermost mantle, where the tomography models have the highest-amplitude heterogeneity, and (2) in the lower mantle, we correct for structure above 500 km above the CMB, well above the strong heterogeneity in the deepest mantle in those models. In fact, mid-lower mantle structure (above our inversion volume) is typically described by very low

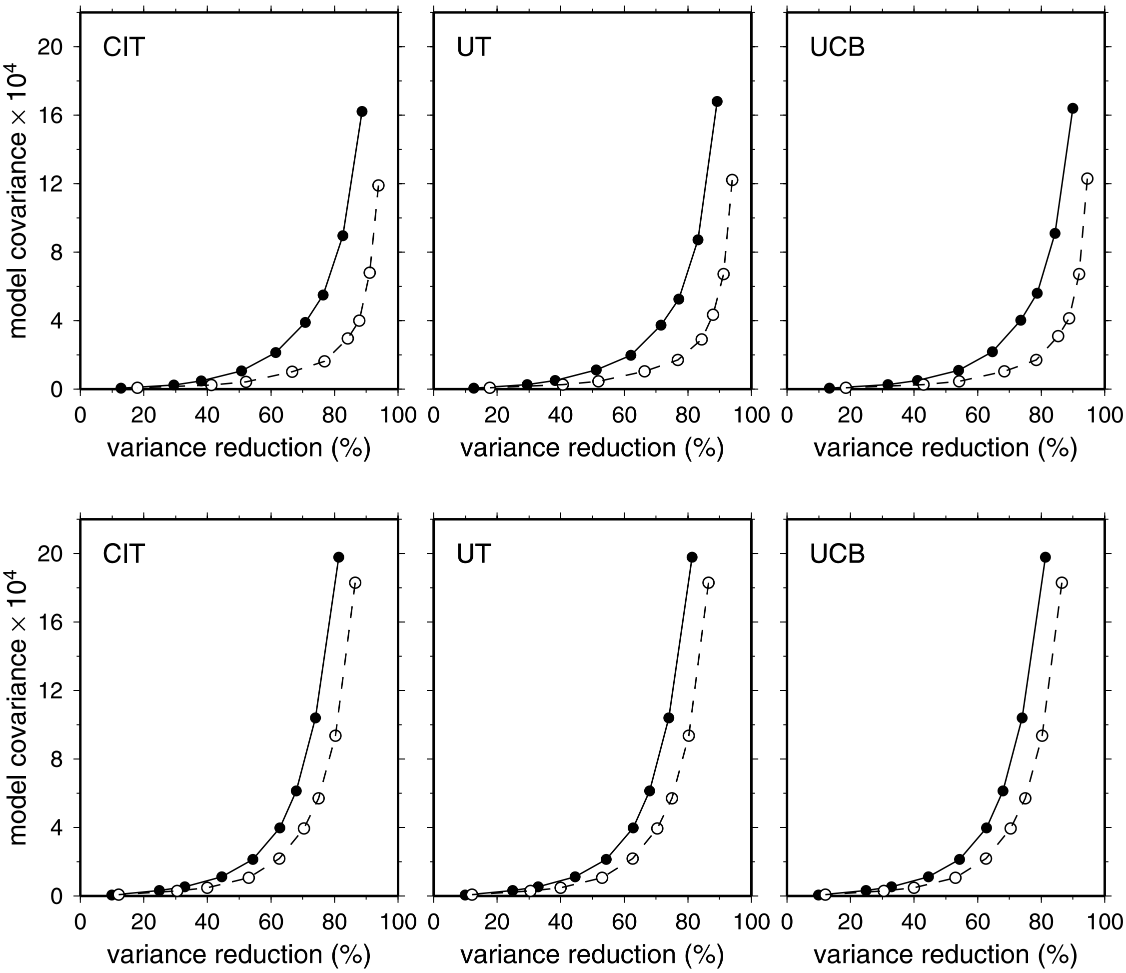

Figure 9. Trade-off relation between data variance reduction and model covariance for the kernel-based models (denoted by solid lines and solid circles) and the ray-based models (denoted by dashed lines and open circles). The three plots on each row are for the three different global models, CIT, UT, and UCB, utilized for correction of mantle heterogeneity. (top) Inversions with no a priori model correlations imposed. (bottom) Model smoothing according to prescribed correlation lengths of ∼60 km in the lateral direction and 50 km in the radial direction.

amplitude heterogeneity in all the models we tested [see, e.g., *Masters et al.*, 2000]. The UCB-corrected travel time data seems to give a slightly better fit but the difference in variance reductions between the three models is insignificant. The velocity models obtained using corrections for the CIT and UT models are provided as auxiliary material (Figures A3–A8).

3.2. Models Based on Onset Versus Peak-to-Peak Travel Times

[20] The 3-D Fréchet kernels are founded on the prerequisite that a finite frequency travel time residual is obtained by cross correlation of an observed broadband waveform with the corresponding synthetic seismogram in a radially symmetric Earth model. We apply the 3-D kernel theory to parametric measurements based on onset and peak-to-peak measurements, not explicit waveform correlations with reference model synthetics. Such measured travel times presumably represent the highest-frequency portions of observed phase arrivals so that infinite frequency ray theory could be considered as a good approximation to interpret actually finite frequency travel times.

[21] To understand the potential difference between the travel times from cross correlation and those from the first-swing alignment, *Hung et al.* [2001] generated a suite of numerical ground truth synthetic waveforms for a homogeneous medium embedded with sphere-shaped anomalies of various sizes and heterogeneity strengths. An automatic cross-correlation procedure and the interactive fitting of the first swings of heterogeneous and homogeneous seismograms are employed to determine the travel time shifts due to the spherical velocity anomalies. The experiments show that the measured travel times based on the first-swing alignment appear to be very similar to those from the peak-to-peak picks, with correlation measurements tending to be slightly smaller values. Namely, the interactive travel time picks can be empirically modeled by the cross-correlation travel times if the latter are computed for sensitivity kernels at an effective period reduced by a factor of 60%. The cross-path width of the effective kernel for a finite frequency travel time determined by the onset time or peak-

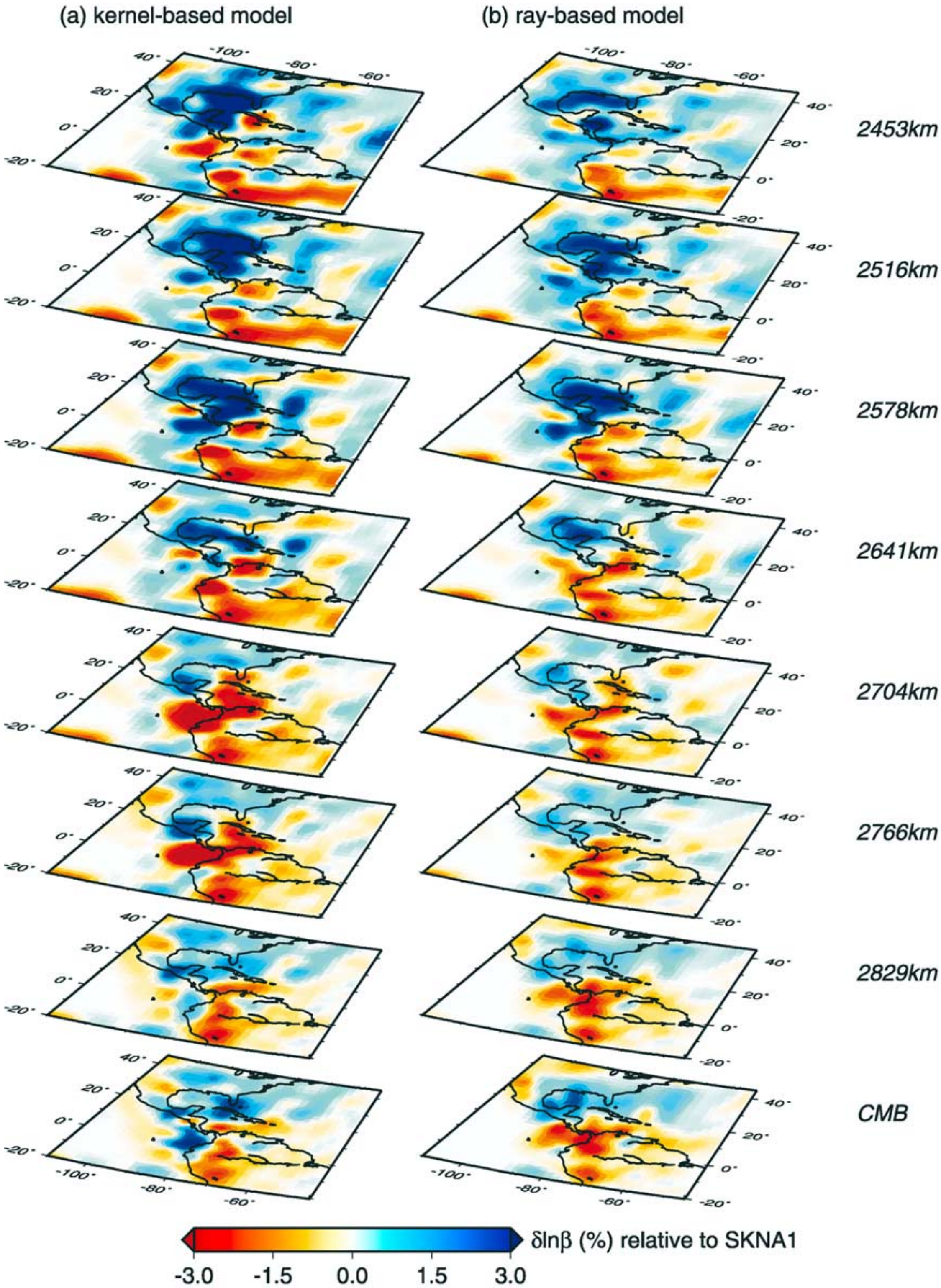

Figure 10. (a) Shear velocity variation relative to the SKNA1 model resolved from finite frequency tomography of the differential travel time residuals corrected using the UCB model. (b) Shear velocity variation relative to the SKNA1 model resolved from ray-based tomography. Each panel illustrates lateral variation in shear velocity perturbation at the depth indicated to the right of the plot. The model is obtained from the damped least squares inversion with additional smoothing regularization in which a priori model correlation lengths of ∼60 km and 50 km are enforced in the lateral and radial dimensions, respectively.

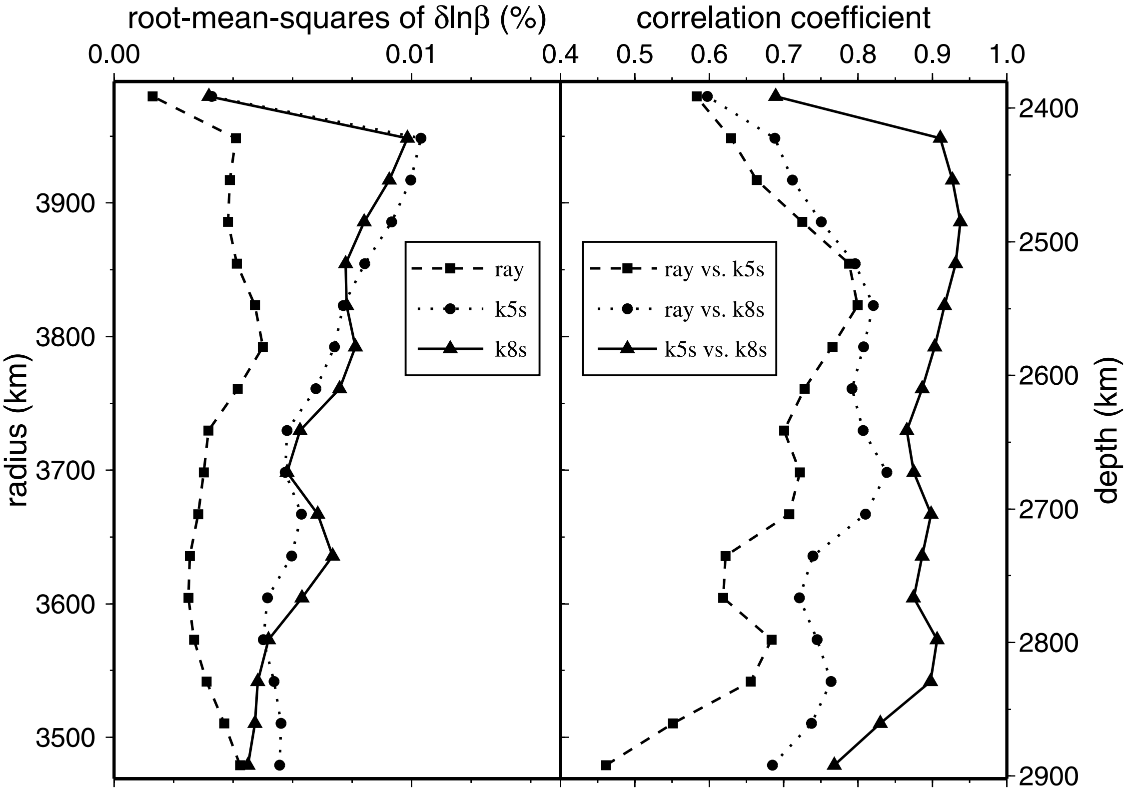

Figure 11. (left) Root-mean-square (RMS) of fractional shear velocity perturbations $\delta\ln\beta$ as a function of radius for the infinite frequency ray model (squares), the 5-s kernel model (circles), and the 8-s kernel model (triangles). (right) Correlation functions on each constant depth nodal grid between two of these three models.

to-peak value could be less than that of the actual Fréchet kernel by a factor of $\sqrt{60} = 77\%$.

[22] As the differential travel time residuals used in our study are based on the peak-to-peak values for (*Scd* + *Sbc*)-*S* and *ScS*-(*Scd* + *Sbc*) data and the onset times for *S*(*Sd*)-*SKS* data, they may preferentially emphasize the higher-frequency arrivals in the observed waveforms whose power spectra have a dominant period of 8 s. Moreover, they suffer the wave front healing effect to some extent different from that undergone by the cross-correlation travel times. To explore the potential influence on the resolved velocity models because of different volumetric sensitivity, we utilize the 3-D kernels with a reduced period of 5 s to conduct the finite frequency tomography as well. In Figure 11 we compare the resulting models with those previously obtained by the 8-s kernels, showing the root-mean-square (RMS) of magnitudes of shear velocity heterogeneity as a function of depth for the three models based on infinite frequency ray theory and the 5- and 8-s kernels. The finite frequency models yield very similar RMS velocity perturbations, approximately 1–2 times larger than those from the ray-based inversion. Figure 11 also shows the correlation function on each constant depth nodal grid between any two of these three models. The higher-frequency, 5-s model shows more resemblance to the ray-based model because ray theory is the infinite frequency limit of Born-Fréchet kernel theory. The two kernel-based models are well correlated at all the depths and reveal very coherent velocity structures except for a localized region near the base of the mantle beneath the middle America (see Figure A9 in the auxiliary material).

3.3. Resolution Tests

[23] We conduct resolution tests to demonstrate the robustness of the solution shear velocity models and to compare the relative merits and differences in recovery of velocity heterogeneity between the kernel- and ray-based tomography. A synthetic model is constructed with four cylindrically shaped, relatively fast or slow velocity anomalies in the D″ region beneath the Caribbean region. Each cylinder has a diameter of 1000 km and height of 250 km placed right above the CMB. The first experiment involves synthetic travel time residuals obtained from the predictions of Born-Fréchet kernel theory inverted for the underlying velocity structure based on the kernel-based tomography (Figure 12a). An alternative experiment uses conventional ray tomography to generate synthetic data that are inverted to resolve the input velocity structure (Figure 12b). Both experiments adopt the DLS solution with the same smoothing regularization as imposed on the real data inversion. The magnitude and geometry of the input velocity anomalies are clearly recovered better in the kernel-based experiment. Vertical smearing is present in both models; however, the ray-based result has more severe horizontal smearing. To assess the resolution of small-scale heterogeneity in the lowermost mantle and possible image artifacts, we conduct a similar test with two groups of narrower and shorter

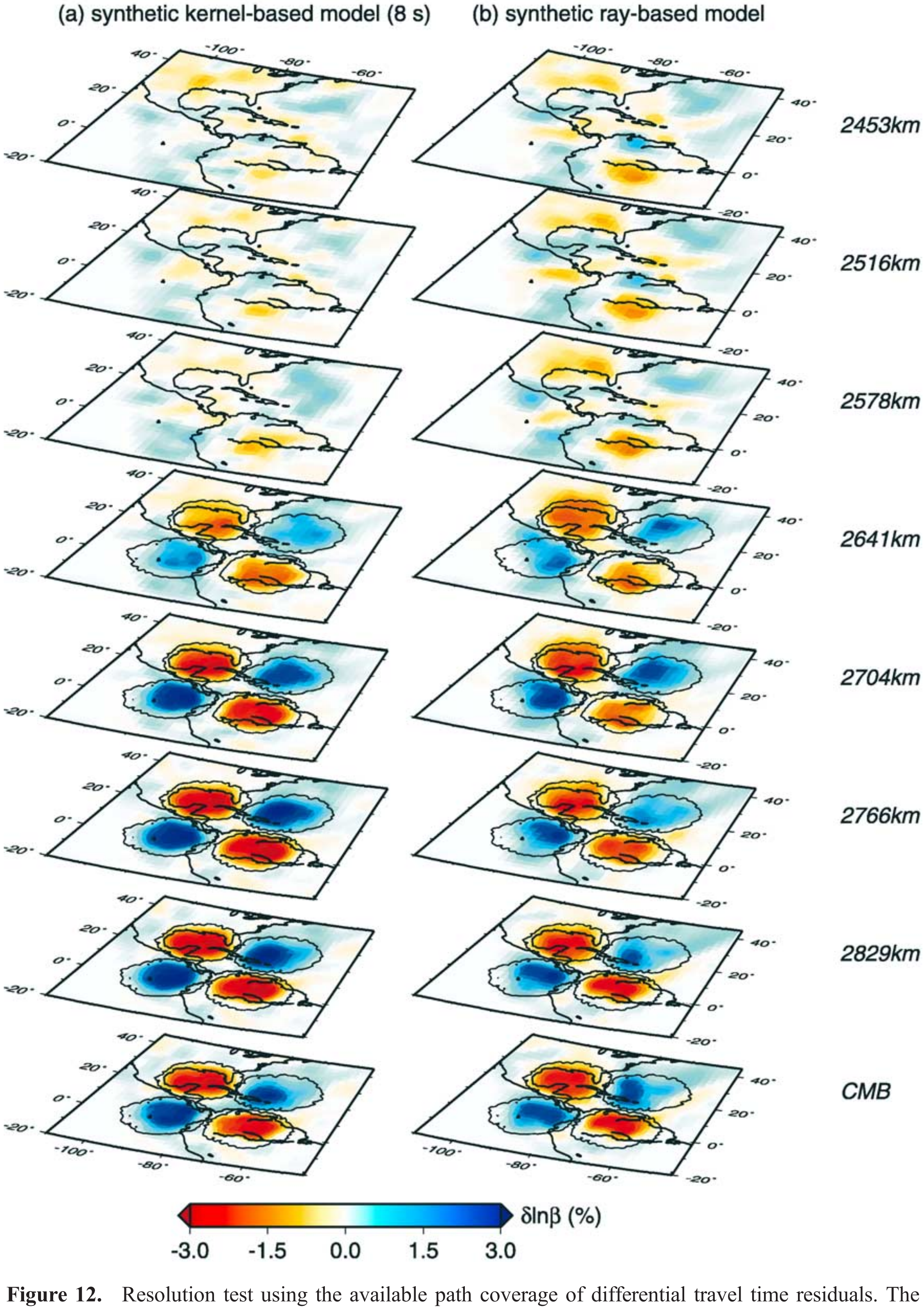

Figure 12. Resolution test using the available path coverage of differential travel time residuals. The input model outlined by the contoured lines has four cylindrically shaped velocity anomalies of either −3% or +3% shear wave velocity perturbations placed in the D″ layer. The cylinders have diameters of 1000 km and heights of 250 km. Both the synthetic data and the data kernels for the inversion are computed using (a) finite frequency kernel theory or (b) infinite frequency ray theory.

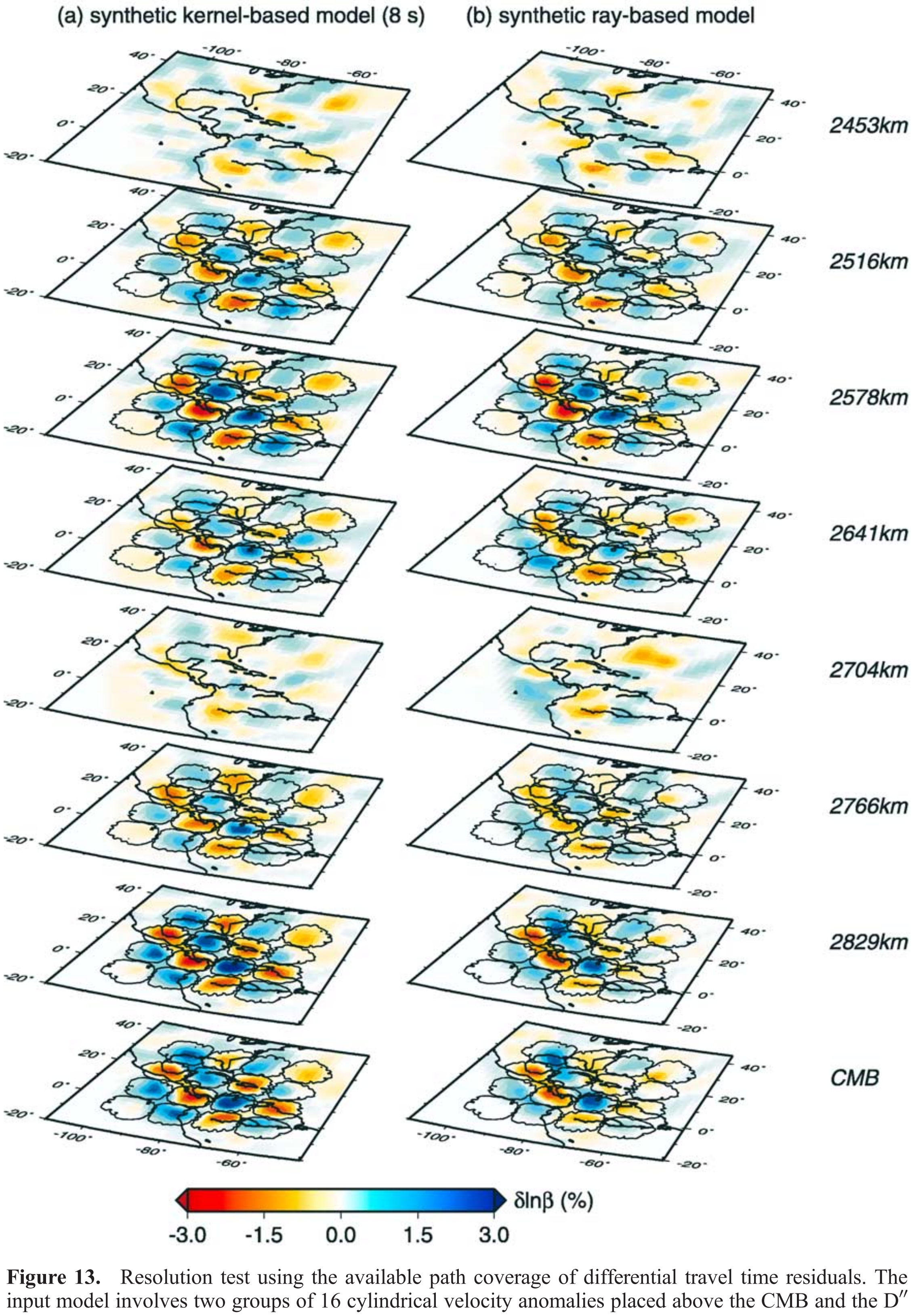

Figure 13. Resolution test using the available path coverage of differential travel time residuals. The input model involves two groups of 16 cylindrical velocity anomalies placed above the CMB and the D″ velocity discontinuity, with the diameter and the height of each cylindrical being half of those in Figure 12. Both the synthetic data and the data kernel for the inversion are computed using (a) finite frequency kernel theory or (b) infinite frequency ray theory.

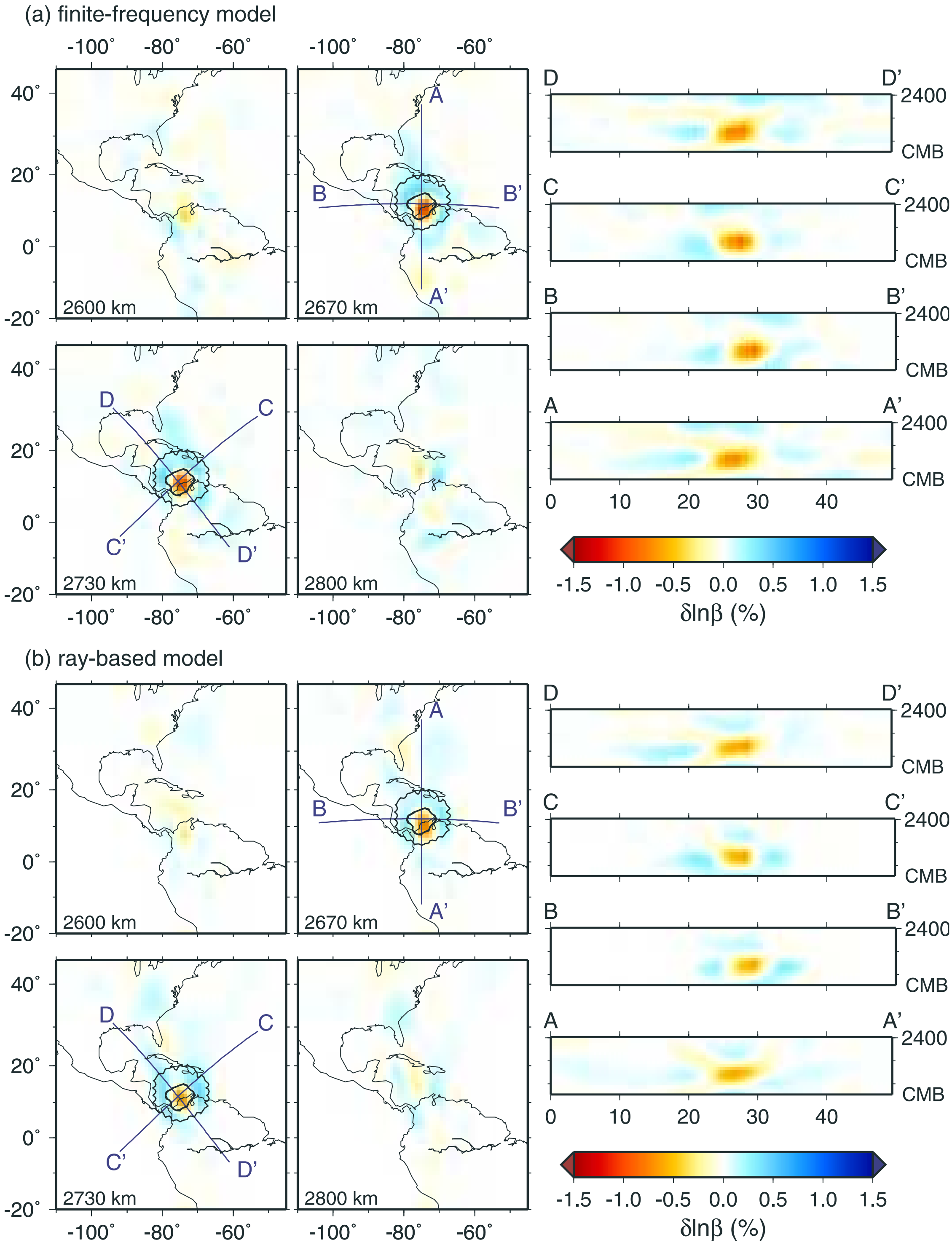

Figure 14. Resolution test using the available path coverage of differential travel time residuals. The input model is a single disk-shaped anomaly of +3% shear velocity perturbations surrounded by a ring of relatively fast anomaly of −3% shear velocity perturbations. The disk has the diameter of 400 km and the height of ∼60 km placed between 2735 and 2798 km below the D″ velocity discontinuity. Both the synthetic data and the data kernel for the inversion are computed using (a) finite frequency kernel theory or (b) infinite frequency ray theory. Note that the scale range, −1.5–1.5%, for the recovered velocity images is only a half of the input heterogeneity strength.

cylindrical anomalies placed right above the CMB and the D″ velocity discontinuity in the input model (500 km and 125 km wide and high, respectively). Similar behavior is seen for the two inversions with superior images for the kernel-based inversion versus the ray-based inversion (Figure 13).

[24] To assess vertical resolution of small-scale low-velocity heterogeneity embedded in the long-wavelength fast velocity structure, we test the synthetic models which have a single disk-shaped slow anomaly of -3% $\delta\beta/\beta$ in the diameter of 400 km and the thickness of 60 km. The disk is centered at (12°N, 75°W) beneath the Caribbean and surrounded by a ring of fast velocity anomaly of +3% $\delta\beta/\beta$. We place this anomalous structure in three different depth ranges which span about two discretized layers: 2735–2798 km below the D″ discontinuity, 2610–2672 km across the D″ discontinuity, and 2484–2547 above the D″ discontinuity. Figure 14 compares the recovered velocity structures based on the sensitivity of 3-D kernels and 1-D rays for the disk located below the D″ discontinuity (see Figures A10 and A11 in the auxiliary material for the other two models). The recovered anomaly in each of the three test models is smeared both laterally and vertically to some extent. The vertical smearing is more severe as the velocity anomaly is placed shallower above the D″ discontinuity. While the resolved magnitude of input velocity heterogeneity is significantly reduced (over 50%) by the smoothing regularization applied in the inversion, the location and the shape of the fine-scale disk structure are fairly well recovered. A classic modeling trade-off is present between constraining discontinuity topography and neighboring volumetric heterogeneity. In this study region, two end-member solutions have been previously pursued: pure D″ topography with no velocity heterogeneity [*Thomas et al.*, 2004], and lateral variations in velocity below a fixed depth discontinuity [*Lay et al.*, 2004a]. In this study, we adopt the approach of fixing discontinuity depth. Since our inversion volume extends to above the D″ reflector, this still allows for high velocities to be mapped above our fixed reflector depth. Though the primary goal in our tomography experiments is to pursue regional heterogeneity in the shear velocity structure.

[25] *Dahlen* [2005] recently derived the Fréchet kernels of finite frequency travel times with respect to 2-D lateral variation in topography of a seismic velocity discontinuity within the Earth. For the travel time of a least time phase like *ScS* and *Sbc* phases, the sensitivity to the discontinuity topography exhibits a doughnut shape around the reflection point and is exactly zero at the ray interaction point. The similarity between the kernel for fractional velocity perturbations and that for discontinuity topography perturbations indicates that there are trade-offs between velocity heterogeneity and topography variations constrained only by differential travel times. Namely, shear velocity heterogeneity imaged under the assumption of a flat D″ discontinuity can be alternatively mapped into lateral variations in topography of the D″ discontinuity if the Earth were radially symmetric. The travel time delay of a shear wave resulting from passage through the slow region can be equivalently associated with the effect from a deeper discontinuity, whereas the faster anomaly and shallower discontinuity lead to the advance of a phase arrival. In a future study we will employ the finite frequency sensitivity kernels for both velocity and discontinuity topography perturbations to simultaneously invert for lateral variations in seismic velocity heterogeneity as well as the topography of the D″ discontinuity.

4. Discussion

[26] We have presented evidence that the tomographic images obtained by the 3-D kernels are superior to those based on ray theory. The resolution tests in Figures 12, 13, and 14 define the region of the model space which is most robust, thus we can now evaluate the model obtained in Figure 10. At depths above the D″ discontinuity there is a strong lateral gradient of 3% to 4% in shear velocity from low-velocity structure beneath South America to high velocity beneath the Gulf of Mexico and Middle America. The latter feature is rather broad, spanning the well-resolved portion of the model, and is not tabular in shape as seen for the upper and midmantle high-velocity structure in models such as those of *Grand* [2002]. Nonetheless, the high-velocity feature is likely to extend vertically upward to the midmantle, suggesting that if this in indeed a relic of the Farallon slab, as advocated by tomographic studies [e.g., *Grand et al.*, 1997], it does reach to at least the top of D″ north of the Caribbean. It is more difficult to assess whether this high-velocity feature is directly related to the origin of the high-velocity layer in D″ (i.e., in reference models like SKNA1). Coupling between the two might be expected if relatively cold slab material accumulated at the base of the mantle gives rise to the high velocity D″ structure. Positive velocity perturbations below the Gulf of Mexico do persist throughout the D″ layer, although these are not as strong as at shallower depths.

[27] The more prominent effect in D″ is associated with the low-velocity perturbations, some of which even reduce the high SKNA velocities by enough to be lower velocity than PREM, more than offsetting the velocity increase of the D″ discontinuity. A localized region of low velocity in D″ beneath Colombia and the Caribbean was previously proposed by *Wysession et al.* [2001] and *Fisher et al.* [2003]. Our tomographic image suggests that this is part of a cluster of low-velocity patches in the vicinity. The D″ high-velocity discontinuity may simply be absent beneath Colombia and the northern Nazca plate, with the inversion offsetting the high-velocity structure of the 1-D reference model. The triplication arrivals only exist at relatively large distances, with any precritical reflections expected to be weak under northern South America, so we cannot directly assess whether the discontinuity is present south of the equator. However, the very localized nature of the low-velocity columns in the D″ images indicates that small-scale structure is embedded in the D″ region on the margin of the relatively uniform, high-velocity region to the north.

[28] If relatively cool, high-viscosity slab material descends to the CMB beneath the Gulf of Mexico, it is likely to displace any hot boundary layer material laterally, and this could trigger boundary layer instabilities along the margins of the slab material [*Tan et al.*, 2002]. The cumulative amount of slab material subducted beneath South America appears to be less than beneath North America, consistent with the lateral gradient in D″ in our

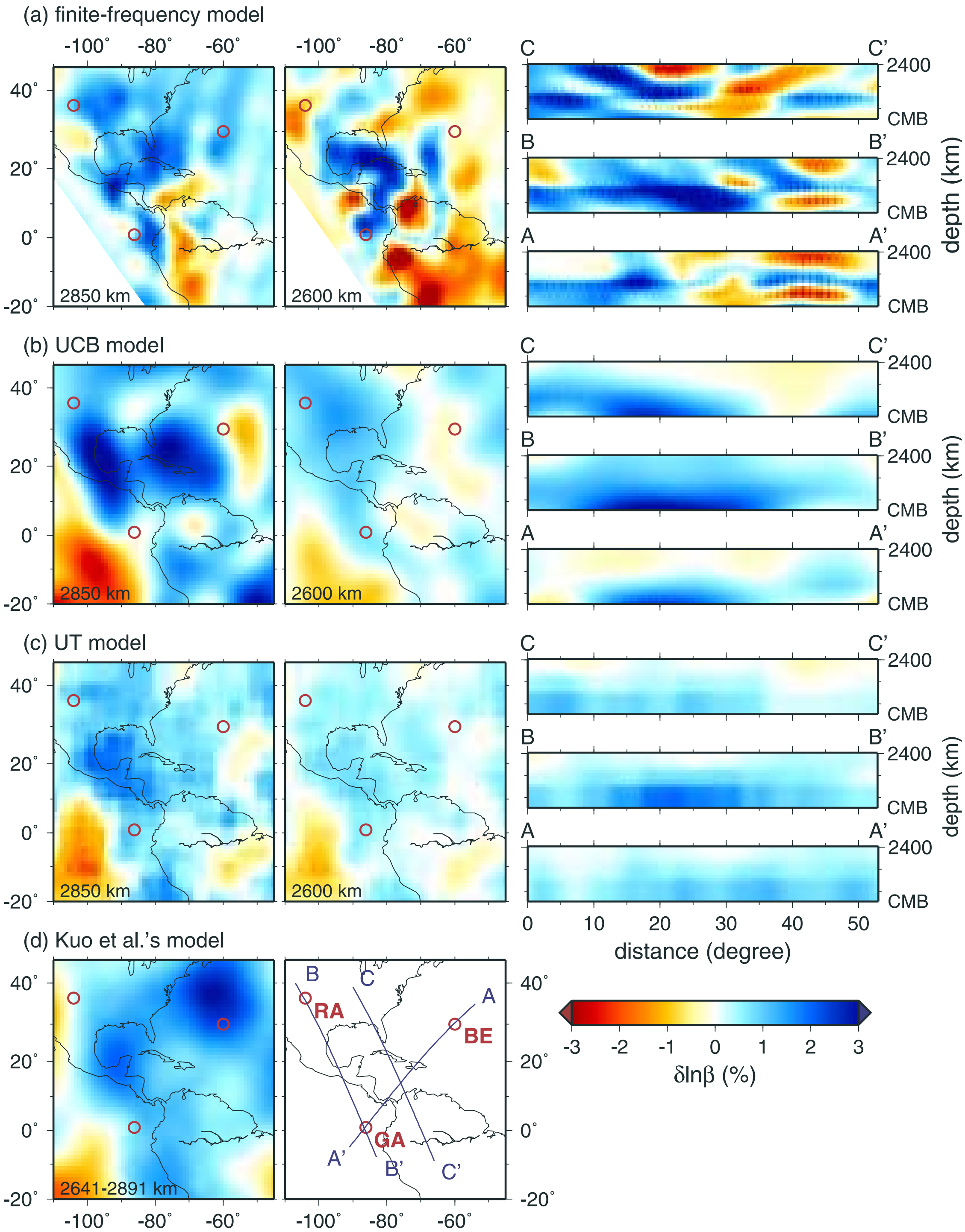

Figure 15. Comparison of shear velocity variation relative to the PREM model from (a) the finite frequency model with that from (b) the UCB model, (c) the UT model, and (d) the D″ model of *Kuo et al.* [2000]. Except for Figure 15d showing a single-layer map of D″ velocity variation, the left two panels of each row illustrate the shear velocity structure at two depths indicated on the maps and on three great circle cross sections, A–A′, B–B′, and C–C′. The middle map of the bottom row indicates the three cross sections denoted by blue lines and the hot spots, Galapagos (GA), Raton (RA), and Bermuda (BE) denoted by open circles [*Muller et al.*, 1993]. Note that the velocity structure in the southwest region lacks resolution and is not shown on the constant depth cross sections.

images [e.g., *Lithgow-Bertelloni and Richards*, 1998]. Ultimately, high-resolution tomography of the entire mantle beneath a downwelling is essential for testing the slab hypothesis fully, and there are other possible explanations for intermittent high-velocity layers in D″ besides accumulated slab material (see *Lay and Garnero* [2004] and *Lay et al.* [2005] for a review of possible scenarios), but two robust deductions can be drawn from our models: (1) There are strong lateral gradients in shear velocity structure both within D″ and within the overlying several hundred kilometers of the lower mantle on scale lengths of 200–500 km, and (2) The circum-Pacific ring of high-velocity structure is not laterally contiguous, as suggested by early low-resolution inversions, but has significant high- and low velocity fluctuations. These observations do tend to support scenarios of dynamical interaction between the mid-mantle and D″, possibly involving slab descent, but further work is needed before a compelling case for this will emerge.

[29] Our solution model is compared to that from global tomographic studies in Figure 15. In map and cross-section view, the predominance of intermediate to short-wavelength structure is apparent in our model compared to the emphasis of longer wavelengths in the global structures. The striking low velocities in our solution images do not exactly correlate with any overlying surface hot spot expression. Recent *P* wave tomography has demonstrated connectivity of low velocities from surface to CMB for many hot spots [*Montelli et al.*, 2004]; the nearest hot spot to our study area is Galapagos, to the west, which connects to low-velocity structure far to the west (~1000 km) of the low velocities imaged here. Thus future work will better assess the possible relationship between the imaged low-velocity anomalies and dynamical scenarios.

[30] D″ beneath the Caribbean has also been mapped to contain seismic anisotropy [e.g., *Kendall and Silver*, 1996; *Garnero and Lay*, 2003]. Our differential times are predominantly dependent on SH structure. Thus in the presence of D″ anisotropy, we are imaging the faster velocity, if the anisotropy geometry is predominantly transverse isotropy with a vertical axis of symmetry. A long-wavelength pattern in azimuthal anisotropy has been put forth for this D″ region [*Garnero et al.*, 2004]. The heterogeneity imaged in our tomography maps is much shorter scale, and thus is likely not strongly affected by such longer-scale trends. We do not anticipate significant contamination of our results by D″ anisotropy, but emphasize we are predominantly modeling the isotropic SH structure.

[31] An important challenge for future work will be to reconcile the strong lateral variations for this region with possible explanations for the origin of the D″ discontinuity. These include a chemically distinct layer [e.g., *Lay et al.*, 2004b], and a mineralogical phase change [e.g., *Murakami et al.*, 2004]. High-resolution seismic analyses hold promise in helping to address this challenge, with the promise of ultralarge data sets from the USArray program.

5. Conclusions

[32] Over 800 high-quality differential travel times have been inverted using ray theory and finite frequency tomography for studying the lowermost mantle beneath the Central America, the Caribbean, and the northernmost South America. Resolution tests indicate our results are robustly constrained in the center of our study area, and that the finite frequency tomography provides improved spatial resolution. In a region characterized by pervasive high velocities in global tomographic imaging, and a first-order D″ discontinuity in regional waveform studies, we map significant high velocities in the bulk of our study region, with significant exceptions beneath portions of the northwestern part of the South American continent. These exceptions consist of localized low velocities that persist vertically through our 500 km thick inversion volume. The high and low velocities may be related to whole mantle dynamics involving ancient subducted material, though such scenarios are not uniquely constrained by our data.

[33] **Acknowledgments.** We thank Sidao Ni and Associate Editor Justin Revenaugh for their thoughtful reviews which improved the manuscript. We also thank Michael Bostock for assistance in acquiring some of the Canadian Seismic Network Data. We thank the IRIS, BDSN, and TERRRascope/Trinet data centers for providing broadband data. This research was supported by National Science Council of the Republic of China under grants NSC93-2119-M-002-031 (S.H.H.), NSC93-2611-M-002-007 (L.Y.C.), and NSC93-2116-M-001-006 (B.Y.K) and NSF grants EAR-0135119 (E.J.G.) and EAR-0125595 (T.L.).

References

Castle, J. C., K. C. Creager, and J. P. Winchester (2000), Shear wave speeds at the base of the mantle, *J. Geophys. Res.*, *105*, 21,543–21,557.
Chiao, L.-Y., and B.-Y. Kuo (2001), Multiscale seismic tomography, *Geophys. J. Int.*, *145*, 517–527.
Dahlen, F. A. (2005), Finite-frequency sensitivity kernels for boundary topography perturbations, *Geophys. J. Int.*, in press.
Dahlen, F. A., S.-H. Hung, and G. Nolet (2000), Fréchet kernels for finite-frequency traveltimes: I. Theory, *Geophys. J. Int.*, *141*, 157–174.
Ding, X., and D. V. Helmberger (1997), Modeling D″ structure beneath Central America with broadband seismic data, *Phys. Earth Planet. Inter.*, *101*, 245–270.
Dziewonski, A. M., and D. L. Anderson (1981), Preliminary reference Earth model, *Phys. Earth Planet. Inter.*, *25*, 297–356.
Dziewonski, A. M., and J. H. Woodhouse (1987), Global images of Earth's interior, *Science*, *236*, 37–48.
Fisher, J. L., M. E. Wysession, and K. M. Fischer (2003), Small-scale lateral variations in D″ attenuation and velocity structure, *Geophys. Res. Lett.*, *30*(8), 1435, doi:10.1029/2002GL016179.
Fukao, Y., S. Widiyantori, and M. Obayashi (2001), Stagnant slabs in the upper and lower mantle transition region, *Rev. Geophys.*, *39*, 291–323.
Garnero, E. J., and T. Lay (2003), D″ shear velocity heterogeneity, anisotropy and discontinuity structure beneath the Caribbean and Central America, *Phys. Earth Planet. Inter.*, *140*, 219–242.
Garnero, E. J., V. Maupin, T. Lay, and M. J. Fouch (2004), Variable azimuthal anisotropy in Earth's lowermost mantle, *Science*, *306*, 259–261.
Grand, S. P. (2002), Mantle shear-wave tomography and the fate of subducted slabs, *Philos. Trans. R. Soc. London, Ser. A*, *360*, 2475–2491.
Grand, S. P., R. D. van der Hilst, and S. Widiyantori (1997), Global seismic tomography: A snapshot of convection in the Earth, *GSA Today*, *7*, 1–7.
Gu, Y. J., A. M. Dziewonski, W. Su, and G. Ekstrom (2001), Models of the mantle shear velocity and discontinuities in the pattern of lateral heterogeneities, *J. Geophys. Res.*, *106*, 11,169–11,199.
Hung, S.-H., F. A. Dahlen, and G. Nolet (2000), Fréchet kernels for finite-frequency traveltimes: II. Examples, *Geophys. J. Int.*, *141*, 175–203.
Hung, S.-H., F. A. Dahlen, and G. Nolet (2001), Wavefront healing: A banana-doughnut perspective, *Geophys. J. Int.*, *146*, 289–312.
Kendall, J.-M., and C. Nangini (1996), Lateral variations in D″ below the Caribbean, *Geophys. Res. Lett.*, *23*, 399–402.
Kendall, J.-M., and P. Silver (1996), Constraints from seismic anisotropy of the nature of the lowermost mantle, *Nature*, *381*, 409–412.
Kuo, B. Y., E. J. Garnero, and T. Lay (2000), Tomographic inversion of S-*SKS* times for shear wave velocity heterogeneity in D″: Degree 12 and hybrid models, *J. Geophys. Res.*, *105*, 28,139–28,157.
Lay, T., and E. J. Garnero (2004), Core mantle boundary structure and processes, in *The State of the Planet: Frontiers and Challenges in Geophysics*, *Geophys. Monogr. Ser.*, vol. 150, edited by R. S. J. Sparks and C. J. Hawkesworth, pp. 25–41, AGU, Washington, D. C.

Lay, T., and D. V. Helmberger (1983), A lower mantle S-wave triplication and the shear velocity structure of D″, *Geophys J. R. Astron. Soc.*, *75*, 799–838.

Lay, T., E. J. Garnero, and S. A. Russell (2004a), Lateral variation of the D″ discontinuity beneath the Cocos plate, *Geophys. Res. Lett.*, *31*, L15612, doi:10.1029/2004GL020300.

Lay, T., E. J. Garnero, and Q. Williams (2004b), Partial melting in a thermo-chemical boundary layer at the base of the mantle, *Phys. Earth Planet. Inter.*, *146*, 441–467.

Lay, T., D. Heinz, M. Ishii, S. Shim, J. Tsuchiya, T. Tsuchiya, R. Wentzcovitch, and D. Yuen (2005), Multidisciplinary impact of the deep mantle phase transition in perovskite structure, *Eos Trans. AGU*, *86*(1), 1, 5.

Lithgow-Bertelloni, C., and M. A. Richards (1998), The dynamics of Cenozoic and Mesozoic plate motions, *Rev. Geophys.*, *36*, 27–78.

Masters, G., H. Bolton, A. M. Dziewonski, and G. Laske (2000), The relative behavior of shear velocity, bulk sound speed, and compressional velocity in the mantle: Implications for chemical and thermal structure, in *Earth's Deep Interior: Mineral Physics and Tomography From the Atomic to the Global Scale*, *Geophys. Monogr. Ser.*, vol. 117, edited by S. Karato et al., pp. 63–87, AGU, Washington, D. C.

Megnin, C., and B. Romanowicz (2000), The three-dimensional shear velocity structure of the mantle from the inversion of body, surface, and higher-mode waveforms, *Geophys. J. Int.*, *143*, 709–728.

Meyerholtz, K. A., G. L. Pavlis, and S. A. Szpakowski (1989), Convolutional quelling in seismic tomography, *Geophysics*, *54*, 570–580.

Montelli, R., G. Nolet, G. Masters, F. A. Dahlen, E. R. Engdahl, and S.-H. Hung (2004), Finite-frequency tomography reveals a variety of plumes in the mantle, *Science*, *303*, 338–343.

Muller, R. D., J.-Y. Royer, and L. A. Lawver (1993), Revised plate motion relative to the hotspots from combined Atlantic and Indian Ocean hotspot tracks, *Geology*, *21*, 275–278.

Murakami, M., K. Hirose, K. Kawamura, N. Sata, and Y. Ohishi (2004), Post perovskite phase transition in $MgSiO_3$, *Science*, *304*, 855–858.

Ni, S., X. Ding, and D. V. Helmberger (2000), Contructing synthetics from deep earth tomographic models, *Geophys. J. Int.*, *140*, 71–82.

Ritsema, J., and H. J. van Heijst (2000), Seismic imaging of structural heterogeneity in Earth's mantle: Evidence for large-scale mantle flow, *Sci. Progr.*, *83*, 1925.

Tan, E., M. Gurnis, and L. Han (2002), Slabs in the lower mantle and their modulation of plume formation, *Geochem. Geophys. Geosyst.*, *3*(11), 1067, doi:10.1029/2001GC000238.

Tanimoto, T. (1990), Long wavelength S velocity structure throughout the mantle, *Geophys. J. Int.*, *100*, 327–336.

Thomas, C., E. J. Garnero, and T. Lay (2004), High-resolution imaging of lowermost mantle structure under the Cocos plate, *J. Geophys. Res.*, *109*, B08307, doi:10.1029/2004JB003013.

Wysession, M. E., K. M. Fischer, G. I. Al-eqabi, P. J. Shore, and I. Gurari (2001), Using MOMA broadband array *ScS-S* data to image smaller scale structures at the base of the mantle, *Geophys. Res. Lett.*, *28*, 867–870.

Zhao, L., T. H. Jordan, and C. H. Chapman (2000), Three-dimensional Fréchet differential kernels for seismic delay times, *Geophys. J. Int.*, *141*, 558–576.

Zienkiewicz, O. C., and R. L. Taylor (1989), *The Finite Element Method*, vol. I, *Basic formulation and Linear Problems*, 4th ed., 648 pp., McGraw-Hill, New York.

L.-Y. Chiao, Institute of Oceanography, National Taiwan University, Taipei, 106, Taiwan.

E. J. Garnero, Department of Geological Sciences, Arizona State University, Tempe, AZ 85287-1404, USA.

S.-H. Hung, Department of Geosciences, National Taiwan University, Taipei, 106, Taiwan. (shung@ntu.edu.tw)

B.-Y. Kuo, Institute of Earth Sciences, Academia Sinica, Nankang, Taiwan.

T. Lay, Institute of Geophysics and Planetary Physics, Earth Sciences Department, University of California, Santa Cruz, CA 95064, USA.